

Robust flat bands of the honeycomb wire network

Chunxiao Liu*

Department of Physics, University of California, Berkeley, California 94720, USA and
Université Paris-Saclay, CNRS, Laboratoire de Physique des Solides, 91405 Orsay, France

Benoît Douçot†

Sorbonne Université, CNRS, Laboratoire de Physique Théorique des Hautes Énergies, LPTHE, F-75005 Paris, France

Jérôme Cayssol‡

Univ. Bordeaux, CNRS, LOMA, UMR 5798, F-33400, Talence, France

(Dated: February 9, 2026)

We show that periodic honeycomb networks of ballistic conducting channels generically host exact flat bands spanning the entire Brillouin zone. These flat bands are independent of microscopic vertex scattering, persist for any number of transverse modes, and occur in a universal 1: 2 ratio with dispersive bands. Their existence is enforced by local D_3 vertex symmetry and lattice translations. We construct compact localized states obeying a Bohr–Sommerfeld-type quantization condition and demonstrate that flat bands survive in realistic antidot lattices, establishing honeycomb wire networks as a robust flat band platform relevant to gated high-mobility 2D electron gases and molecule-patterned metallic surfaces.

Introduction. In periodic media, the behavior of excitations is governed by the underlying band structure of the energy spectrum [1]. While generic systems exhibit dispersive bands separated by gaps, the possibility to engineer flat bands (FBs), characterized by vanishing group velocities, challenges our paradigms on quantum transport and phase transitions because the quenching of kinetic energy enhances the effects of quantum geometry [2], Coulomb interaction [3, 4] and disorder [5]. Besides the Landau levels of the quantum Hall effect [1, 6], FBs and their associated compact localized states (CLS) can arise from destructive interference of hopping processes in frustrated lattices [7–11], without requiring any magnetic field. This caging effect has been realized across a wide range of platforms [12, 13], including electronic materials [14, 15], plasmonic arrays [16], resonator networks [17], and lattices with various elementary constituents: cold-atoms [18, 19], photons [20–23], polaritons [24] and phonons [25]. More recently, the emergence of FBs has been systematically investigated within discrete tight-binding models [26–29] or equivalently combinatorial graphs [30].

Continuous differential operators acting along one-dimensional quantum graphs (QGs) [31, 32] have been used to modelize aromatic molecules [33, 34], arrays of 1D metallic wires [35, 36], percolation in various contexts [37–41], quantum chaos [42–45], and even finite order approximations to fractals [46, 47]. In contrast to tight-binding systems, there are very scarce occurrences of FBs in periodic QGs, a notable exception being the honeycomb quantum graph (HQG) [48, 49]. In some moiré materials [50–53], chiral edge states can realize

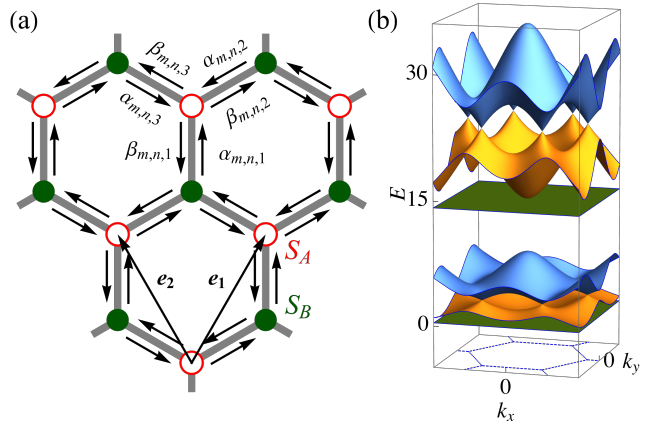


Figure 1. (a) The single channel honeycomb wire network, with translation vectors $e_{1,2}$. Each wire contains two counter-propagating plane waves with amplitude $\alpha_{m,n,i}$ and $\beta_{m,n,i}$. Elastic scattering happens at the nodes, described by scattering matrices S_A for sublattice A (open red) and S_B for sublattice B (filled green). (b) Energy spectrum of the honeycomb wire network as a function of the Bloch momentum \mathbf{k} in the Brillouin zone (dashed blue hexagon). Flat bands (green) are observed for any S_A and S_B , the particular scattering parameters being here $(\theta_v, \phi_v) = (\pi/9, 4\pi/5)$ for both $v = A, B$, see Eq. (4).

such HQG in the single channel case. It is therefore natural to investigate whether such FBs can also pertain in nano-assembled arrays of metallic wires or patterned two-dimensional electron gas (2DEG) [54, 55], situations where each bond harbors a large number of transverse modes coupled through the vertex connections.

In this letter, we show that any honeycomb array of ballistic multichannel wires harbors robust flat bands

* chunxiao.liu@universite-paris-saclay.fr

† benoit.doucot@sorbonne-universite.fr

‡ jerome.cayssol@u-bordeaux.fr

which extend over the whole Brillouin zone, regardless of the details of the inter-wire connections. The latter solely affect the common energy and the nodal structure of the hexagonal CLS without destroying their exact degeneracy, which is protected by the D_3 symmetry of the honeycomb structure. We also investigate a more realistic 2D antidot array where electrons are forced to avoid hexagonal obstacles, and which is shown to also host FBs in regimes beyond the strict HQG case. This paves the way for experimental realizations through various modern nanotechnology techniques, including i) high-mobility semiconducting or graphene based 2DEG gated by honeycomb shaped metallic grids, or ii) a very clean (111) Cu surface where hexagonal clusters of CO molecules are artificially deposited by a STM tip [46, 47]. We emphasize that these FBs of the HQG differ from graphyne [56, 57] and from the superlattices of twisted bilayer graphene [58].

The single channel case in momentum space. We study the Schrödinger differential operator $H = -\hbar^2/(2m)d^2/ds^2$ along the HQG, where $s \in (0, a_0)$ denotes the continuous local coordinate defined on each bond, as the distance from B site. For the rest of the paper we set $E_0 \equiv \hbar^2/(2m) = 1$ and $a_0 = 1$. We consider solely elastic scattering at the nodes described by 3 by 3 scattering matrices S_v , indexed by the sublattice index $v = A, B$. The bond index $\mathbf{l} = (m, n, i)$ encapsulates the leg index $i \in \{1, 2, 3\}$, and the integer coordinates $(m, n) \in \mathbb{Z}^2$ for the unit cell (Fig. 1). The scalar wave function $\Psi_{\mathbf{l}}(s)$ at energy E inside bond $\mathbf{l} = (m, n, i)$ is a linear superposition of two counterpropagating plane waves :

$$\Psi_{\mathbf{l}}(s) = \alpha_{\mathbf{l}} e^{iqs} + \beta_{\mathbf{l}} e^{-iqs}, \quad (1)$$

where $q > 0$ is the longitudinal wave vector along the bond, and $E = q^2$. Taking advantage of the invariance under lattice translations, we further performed the Bloch reduction $(m, n) \rightarrow \mathbf{k}$ by introducing a Bloch wave vector \mathbf{k} [59]. The scattering conditions at vertices A ($s = 1$) and B ($s = 0$) read :

$$\begin{pmatrix} |\alpha_{\mathbf{k}}\rangle \\ |\beta_{\mathbf{k}}\rangle \end{pmatrix} = \begin{pmatrix} 0 & D_{\mathbf{k}}^\dagger S_B D_{\mathbf{k}} \\ e^{2iq} S_A & 0 \end{pmatrix} \begin{pmatrix} |\alpha_{\mathbf{k}}\rangle \\ |\beta_{\mathbf{k}}\rangle \end{pmatrix}, \quad (2)$$

where the vector $|\alpha_{\mathbf{k}}\rangle = (\alpha_{\mathbf{k},1}, \alpha_{\mathbf{k},2}, \alpha_{\mathbf{k},3})$ represents the mode propagating from B to A , while $|\beta_{\mathbf{k}}\rangle = (\beta_{\mathbf{k},1}, \beta_{\mathbf{k},2}, \beta_{\mathbf{k},3})$ represents the mode propagating from A to B . The diagonal matrix $D_{\mathbf{k}}$ with diagonal entries $(1, e^{-i\mathbf{k}\cdot\mathbf{e}_1}, e^{-i\mathbf{k}\cdot\mathbf{e}_2})$ accounts for the Bloch phase shifts between different unit cells. The condition for a non-trivial solution of Eq. (2) is expressed by the following eigenproblem :

$$e^{2iq(E)} D_{\mathbf{k}}^\dagger S_B D_{\mathbf{k}} S_A |\alpha_{\mathbf{k}}\rangle = |\alpha_{\mathbf{k}}\rangle, \quad (3)$$

where $q = q(E) = \sqrt{E}$. Solving the corresponding determinant secular equation provides the full band structure

of HQG, which consists of 3 branches of e^{iq} vs \mathbf{k} , yielding an infinite spectrum of discrete levels q (or E) for each \mathbf{k} . Note that this quantum graph construction, and specifically Eq. (3), apply to any bipartite lattice.

We now explain that the particular D_3 symmetry around each vertex of HQG implies that one of the 3 energy branches is always a FB. Indeed, the scattering matrix S_v is an element of the quotient group $U(3)/D_3$ and has therefore the very particular spectral decomposition [60]:

$$S_v = e^{i\phi_v} P_{\perp} + e^{i\theta_v} P_{\parallel}, \quad (4)$$

where the eigenvalue $e^{i\theta_v}$ is associated with the rank-1 projector P_{\parallel} along the vector $|e_3\rangle = (1, 1, 1)/\sqrt{3}$, while eigenvalue $e^{i\phi_v}$ is attached to the rank-2 projector $P_{\perp} = \mathbb{I}_3 - P_{\parallel}$ onto the subspace orthogonal to $|e_3\rangle$.

Obtaining FBs consists in finding, for each Bloch wave vector \mathbf{k} , a nontrivial vector $|\alpha_{\mathbf{k}}\rangle$ that solves the eigenproblem (3) with a value of q *independent* of \mathbf{k} . The solution is not guaranteed to exist for arbitrary bipartite lattice because the scattering matrices do not commute with $D_{\mathbf{k}}$. Nevertheless, a FB solution does exist for the HQG due to the specific two-projector structure of Eq. (4). Indeed for any \mathbf{k} , one can always choose a vector $|\alpha_{\mathbf{k}}\rangle$ such that $|\alpha_{\mathbf{k}}\rangle \in \text{Im}P_{\perp}$ and $D_{\mathbf{k}}|\alpha_{\mathbf{k}}\rangle \in \text{Im}P_{\perp}$. Then for such states, the matching Eq. (3) reduces to :

$$e^{i(2q+\phi_A+\phi_B)} |\alpha_{\mathbf{k}}\rangle = |\alpha_{\mathbf{k}}\rangle \quad (5)$$

since $D_{\mathbf{k}}^\dagger D_{\mathbf{k}} = \mathbb{I}_3$, and therefore

$$2q + \phi_A + \phi_B = 2\pi\mathbb{Z}, \quad \forall \mathbf{k} \in \text{BZ}. \quad (6)$$

The momentum q and the energy $E = q^2$ are now \mathbf{k} -independent, hence the FB, although the eigescattering vector $|\alpha_{\mathbf{k}}\rangle$ forms a texture winding as a function of \mathbf{k} [59]. This leads to an infinite set of *exact flat bands extending within the whole Brillouin zone*. Hence, even for arbitrary values of θ_v and ϕ_v , Eq. (6) coincides with the Bohr-Sommerfeld quantization rule one would have for the very particular case of perfect mirrors, namely when $\theta_v = \phi_v$ and $S_v = e^{i\phi_v} \mathbb{I}_3$, since $2q + \phi_A + \phi_B$ is the phase accumulated along a closed semi-classical trajectory. Note that the energy of the FBs depends only on the angular parameters ϕ_v ($v = A, B$), and not on θ_v , which affect solely the dispersive bands. Previous works [48] treated the case where both wave functions and their derivatives are continuous at A and B sites, the so-called Neumann boundary conditions, which correspond to the very specific parameters $(\theta_v, \phi_v) = (0, \pi)$ for $v = A, B$. Throughout our analysis we allow for different scattering matrices, S_A and S_B , at A -type and B -type vertices, which generalizes previous work assuming $S_A = S_B$ [51] to staggered or Kekulé honeycomb lattices. The two-projector structure that leads to the FBs of HQG can also be employed to argue for FBs in the tight binding model for Kagome ($S_A = S_B$) and breathing Kagome [61, 62] ($S_A \neq S_B$).

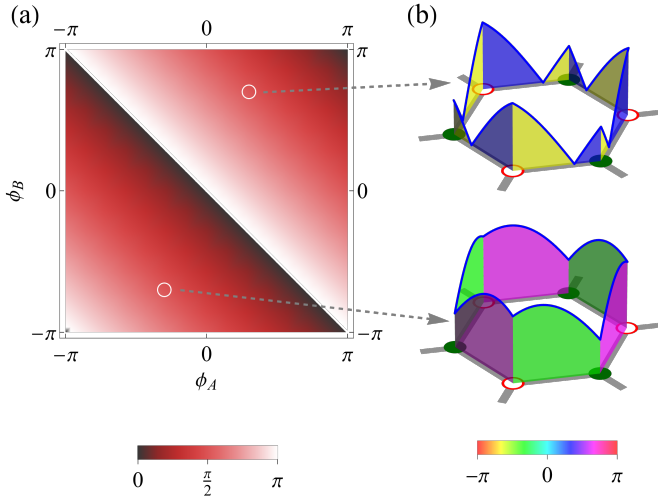


Figure 2. Data of the lowest energy compact localized states (CLSSs): (a) The value of the 1D wave vector q (shown as color) of the CLSSs as a function of $\phi_{A,B}$: $q/\pi \equiv -\frac{\phi_A + \phi_B}{2\pi} \bmod 1$, and (b) Two representative CLSSs corresponding to the values $(\phi_A, \phi_B) = \pm(3\pi/10, 7\pi/10)$, where the amplitude of the wave function is shown as the height, and the argument as the color. A CLS in the lower left (upper right) triangle region of (ϕ_A, ϕ_B) parameter space in (a) has zero (one) node: this is manifest in the CLSs shown in (b).

Compact localized states. Since the extended Bloch states forming the FB are degenerate in energy, their superpositions are still eigenstates and can have compact supports [63–66]. Here we build explicitly the CLS corresponding to the FBs Eq. (6) of the HQG by following three steps. First, we set all the amplitudes $\alpha_{m,n,i}$ and $\beta_{m,n,i}$ to zero everywhere over the HQG, except on a selected hexagon (Fig. (2)). Second, we choose the remaining amplitudes to follow the alternating pattern $(\alpha_b, \beta_b) = (\alpha, \beta)(-1)^b$, around the hexagon, where $b = 0, \dots, 5$ is a bond index. As a result, any scattering in- or out- state at any corner of the hexagon looks like $|\alpha\rangle_v = \alpha(1, -1, 0)$ or a circular permutation, and similarly $|\beta\rangle_v = \beta(1, -1, 0)$ or a circular permutation. We observe that such vectors span the plane orthogonal to $|e_3\rangle = (1, 1, 1)/\sqrt{3}$. Therefore the action of the $S_{A,B}$ matrices on such in- and out-scattering states is very simple, and leads to a single scalar equation $\beta = e^{2iq + i\phi_A}\alpha$ at the 3 A -corners of the selected hexagon, and $\alpha = e^{i\phi_B}\beta$ at all the 3 B -corners. Combining those two equations leads directly to Eq. (6) already obtained in the Bloch representation. Since this construction can be performed for any hexagon, it is an alternative proof of the existence of FBs ruled by the Bohr–Sommerfeld condition (6). For the particular case of Neumann boundary conditions $\phi_A = \phi_B = \pi$, we recover the Dirichlet eigenstates [48] where the CLS have nodes at vertices. More generally, one can follow the number and locations of the nodal points in the CLS, depending on the FB number n and on the parameters (ϕ_A, ϕ_B) . It is possible to go from CLS to Bloch scattering states by summing the CLS over unit cells with

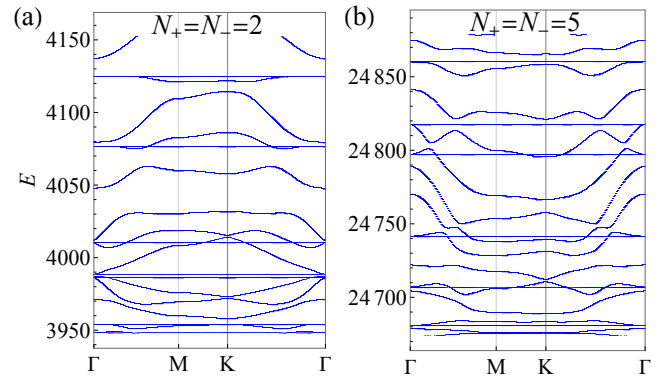


Figure 3. The spectrum along high symmetry path in the Brillouin zone for the N -channel honeycomb quantum graph with $N = N_+ + N_-$: (a) $N_\pm = 2$, (b) $N_\pm = 5$. We take arbitrary parametrization following Eq. (8) for the scattering matrices $S_{A/B}$ at the nodes, and assume the μ -th channel has the energy-momentum relation $E = q_\mu^2 + (\pi\mu/w)^2$. We take $w = 0.2$.

appropriate phase, and vice versa. It is interesting to note that both the FBs and the CLSs discussed above are robust to the introduction of a longitudinal localized potential $V(s)$ acting on the bonds, thereby generalizing the results of [48] which considered symmetric $V(s)$ with respect to the center of a bond.

Multichannel model with a sharp transverse confining potential. Typical experimental settings of HQG involve multiple transverse channels due to the wire width w . To model such more realistic situations, we introduce local coordinates for each bond $\mathbf{s} = (s, s_\perp)$ that gather the longitudinal coordinate s and the transverse one $s_\perp \in [-w/2, w/2]$ with respect to its axis. Using strict boundary conditions, corresponding to an infinite potential well in the s_\perp direction, the wave function $\Psi_l(\mathbf{s}) = \Psi_l(s, s_\perp)$ reads :

$$\Psi_l(\mathbf{s}) = \sum_{\mu=1}^N \alpha_{\mu,l} e^{iq_\mu s} \Phi_\mu(s_\perp) + \beta_{\mu,l} e^{-iq_\mu s} \Phi_\mu^*(s_\perp), \quad (7)$$

where the transverse envelope functions $\Phi_\mu(s_\perp)$ vanish at the lateral walls of each wire : $\Phi_\mu(w/2) = \Phi_\mu(-w/2) = 0$. The sum is over the $N = 1 + \text{Int}[q(E)w/\pi]$ transverse channels, labelled by the integer index μ and carrying longitudinal momenta $q_\mu(E) = \sqrt{E - (\pi\mu/w)^2}$. Owing to mirror symmetry with respect to each wire axis, $(s, s_\perp) \rightarrow (s, -s_\perp)$, the transverse modes are classified in two categories according to their parity : N_+ even modes and N_- odd modes, with $N = N_+ + N_-$. At vertex $v = A, B$, the multichannel scattering matrix S_v belongs to $U(3N)/D_3$. Using group theory (see [59] for details) we obtain the tensor decomposition :

$$S_v = S_{v,0} \otimes P_\perp + \text{diag}(S_{v,+}, S_{v,-}) \otimes P_\parallel. \quad (8)$$

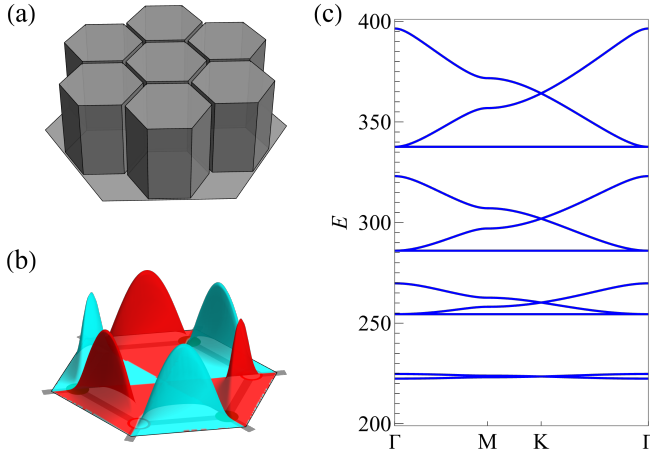


Figure 4. (a) The antidots potential profile (see Eq. (10)); the narrow potential-free region ($V = 0$) appears as trenches between barrier regions ($V = V_0$), forming a quasi-1D hexagonal network of width w . (b) The 2D compact localized state (CLS) around one hexagon solved from the antidot potential in (a). The amplitude and phase of the wave function are shown as the height and color, respectively; the latter follows the colorbar in Fig. 2(b). (c) Low energy spectrum of the antidot model along high symmetry path in the Brillouin zone. All panels are plotted with parameters $(V_0, w) = (400, \sqrt{3}/20)$.

Here the projectors P_{\perp} and P_{\parallel} (see Eq. (4)) act in the wire/leg space while $S_{v,0} \in U(N)$ and $\text{diag}(S_{v,+}, S_{v,-}) \in U(N_+) \oplus U(N_-)$ act in the transverse channel space; the block-diagonal structure of $S_{v,\pm}$ shows that mixing between even and odd subspaces are forbidden for the P_{\parallel} sector by the D_3 symmetry. The multichannel secular equation is a direct generalization of the single channel case Eq. (3) and reads

$$\det \left((e^{iQ(E)} \otimes D_{\mathbf{k}}^{\dagger}) S_B (e^{iQ(E)} \otimes D_{\mathbf{k}}) S_A - \mathbb{I}_{3N} \right) = 0, \quad (9)$$

where $Q = \text{diag}(q_1, q_3, \dots, q_{2N_+ - 1}, q_2, q_4, \dots, q_{2N_-})$ collects the propagating wave vectors of the odd- and even-parity channels.

A natural question concerning FBS is whether they persist in the multichannel case. To answer this, we plot in Fig. 3 the low energy spectrum obtained from numerically solving the secular equation (9) for two representative cases $N_{\pm} = 2$ and $N_{\pm} = 5$, with arbitrary scattering matrices chosen according to Eq. (8). Remarkably, we observe multiple FBS in both cases; furthermore, they appear in a ratio of one FB for two dispersive ones, suggesting that FBS are ubiquitous and have a prescribed density in the spectrum. Indeed, we prove in [59] that the existence of FBS is a direct consequence of the D_3 symmetry and the decomposition Eq. (8). Finally an argument using random matrix theory is used to characterize the density of the FBS. We expect all these results to hold for HQG with arbitrarily large number of channels, which is relevant for clean metallic wires.

Flat bands in a patterned 2DEG in presence of an

antidot potential $V(x, y)$. The multichannel problem considered above demonstrates the robustness of FBS in realistic 1D HQGs with finite width, relevant for metallic arrays. Below we consider a more general setting where a continuous high mobility 2DEG is patterned by an external periodic antidot potential $V(x, y)$. By gating, the electron gas is depleted in the core of the hexagons and forces the electrons to flow along channels in-between the hexagons, thereby approaching the 1D HQG as a limit. It can also be realized, alternatively, by artificially depositing molecules along hexagonal clusters on top of a Cu clean surface [46, 67]. The model is the standard 2D Schrödinger equation $H = -\partial_x^2 - \partial_y^2 + V(x, y)$ with

$$V(x, y) = \begin{cases} V_0, & (x, y) \in \bigcup_{m,n \in \mathbb{Z}} \bullet_{(m,n), 1-w/\sqrt{3}}, \\ 0, & \text{otherwise,} \end{cases} \quad (10)$$

where (x, y) are the global cartesian coordinates in the plane, and $\bullet_{(m,n),h}$ denotes a hexagonal region centered at $me_1 + ne_2$ with side length h , see Fig. 4(a) for an illustration. For sufficiently high (i.e. large V_0) and narrow (i.e. small w) barriers, the spectrum contains extended states at high energy $E \gtrsim V_0$, and bound states at energy $V_0 \geq E \gtrsim \pi^2/w^2$ associated with the propagation along the potential-free, quasi-1D hexagonal network. The HQG is reproduced in the $V_0 \rightarrow \infty, w \rightarrow 0$ limit, where FBS exist. On the other hand, the free 2DEG ($w \rightarrow \sqrt{3}, V_0 \rightarrow 0$) does not admit any FBS. This raises the following questions: do FBS persist in the spectrum outside the HQG regime, and can we predict the flatness of the bands upon varying w and V_0 ?

To answer these questions, we first study the model (10) at representative parameters $(V_0, w) = (400, \sqrt{3}/200)$. We plot in Fig. 4(c) the spectrum along high symmetry path, where several bands are visibly flat, with the largest bandwidth $\Delta_{\text{FB}} = 0.004$. These approximately flat bands can be adiabatically traced to the FBS in the limit $V_0 \rightarrow \infty, w \rightarrow 0$, yet the corresponding 1D HQG picture (assuming the same width w) would predict a much larger energy for the lowest FB $\pi^2/w^2 \approx 1316$, showing the limitation of the HQG picture in understanding the current parameter regime. This analysis, together with the smallness of Δ_{FB} , demonstrates the remarkable robustness of FBS *beyond* the 1D HQG regime. We then track the band width as a function of w and V_0 [59], and obtain the empirical law that approximately flat bands exist within a range of $\sqrt{V_0 - 80 - 1.5/w^2}(\sqrt{3} - w)^9 \gtrsim 150$.

We further solve the antidot problem in real space with Dirichlet boundary conditions to obtain the 2D CLS associated with the lowest approximately flat band, see Fig. 4(b). The CLS has nodes at the vertices, reminiscent of the Dirichlet eigenstates [48] of the HQG associated with the Neumann boundary conditions $\phi_A = \phi_B = \pi$. We mention that across all parameter values, the lowest two bands always give rise to 0D bound states at the nodes. The detailed study can be found in [59].

Conclusion. Using the honeycomb design, FBS can be obtained generically in clean 2DEG patterned by anti-

dots or gating, or in metallic wire networks regardless of the details of the connections. We have also obtained similar FBs for the 3D diamond structure, being the 3D counterpart of the honeycomb structure.

In addition to gated high-mobility 2DEGs and molecule-patterned metallic surfaces, our proposed FBs can also be naturally realized in photonic and phononic crystals, microwave and optical waveguide networks, artificial graphene, engineered metamaterials. Concerning electronics, our model can be used to study correlation effects including superconductivity and spin liquids, and explore

the interplay between flat bands and correlations in moiré graphene [68], rhombohedral graphite [69] and kagome metals [70]. Another interesting perspective concerns the disorder effects on FBs, localization (or antilocalization) effects and quantum transport outside the ballistic regime.

Acknowledgements. We thank Jean-Noël Fuchs for discussions about the antidot model. JC thanks Joel Moore and UC Berkeley physics department for hospitality, in the framework of the Fulbright program 2025. CL was supported by the U.S. Department of Energy, Office of Science, National Quantum Information Science Research Centers, Quantum Science Center.

[1] S. M. Girvin and K. Yang, *Modern Condensed Matter Physics* (Cambridge University Press, 2019).

[2] P. Törmä, Essay: Where can quantum geometry lead us?, *Phys. Rev. Lett.* **131**, 240001 (2023).

[3] O. Derzhko, J. Richter, and M. Maksymenko, Strongly correlated flat-band systems: The route from heisenberg spins to hubbard electrons, *International Journal of Modern Physics B* **29**, 1530007 (2015).

[4] J. G. Checkelsky, B. A. Bernevig, P. Coleman, Q. Si, and S. Paschen, Flat bands, strange metals and the kondo effect, *Nature Reviews Materials* **9**, 509 (2024).

[5] T. Bilitewski and R. Moessner, Disordered flat bands on the kagome lattice, *Phys. Rev. B* **98**, 235109 (2018).

[6] K. von Klitzing, G. Dorda, and M. Pepper, New Method for High-Accuracy Determination of the Fine-Structure Constant Based on Quantized Hall Resistance, *Phys. Rev. Lett.* **45**, 494 (1980).

[7] B. Sutherland, Localization of electronic wave functions due to local topology, *Phys. Rev. B* **34**, 5208 (1986).

[8] A. Mielke, Ferromagnetism in the hubbard model on line graphs and further considerations, *Journal of Physics A: Mathematical and General* **24**, 3311 (1991).

[9] A. Mielke, Exact ground states for the hubbard model on the kagome lattice, *Journal of Physics A: Mathematical and General* **25**, 4335 (1992).

[10] H. Tasaki, Ferromagnetism in the hubbard models with degenerate single-electron ground states, *Phys. Rev. Lett.* **69**, 1608 (1992).

[11] J. Vidal, R. Mosseri, and B. Douçot, Aharonov-bohm cages in two-dimensional structures, *Phys. Rev. Lett.* **81**, 5888 (1998).

[12] D. Leykam, A. Andreanov, and S. Flach, Artificial flat band systems: from lattice models to experiments, *Advances in Physics: X* **3**, 1473052 (2018).

[13] D. Leykam and S. Flach, Perspective: Photonic flatbands, *APL Photonics* **3**, 070901 (2018).

[14] I. Hase, T. Yanagisawa, Y. Aiura, and K. Kawashima, Possibility of flat-band ferromagnetism in hole-doped pyrochlore oxides $\text{sn}_2\text{nb}_{207}$ and $\text{sn}_2\text{ta}_{207}$, *Phys. Rev. Lett.* **120**, 196401 (2018).

[15] M. Kang, L. Ye, S. Fang, J.-S. You, A. Levitan, M. Han, J. I. Facio, C. Jozwiak, A. Bostwick, E. Rotenberg, M. K. Chan, R. D. McDonald, D. Graf, K. Kaznatcheev, E. Vescovo, D. C. Bell, E. Kaxiras, J. van den Brink, M. Richter, M. Prasad Ghimire, J. G. Checkelsky, and R. Comin, Dirac fermions and flat bands in the ideal kagome metal fesn, *Nature Materials* **19**, 163 (2020).

[16] Z. Xu, X. Kong, J. Chang, D. F. Sievenpiper, and T. J. Cui, Topological flat bands in self-complementary plasmonic metasurfaces, *Phys. Rev. Lett.* **129**, 253001 (2022).

[17] D. L. Underwood, W. E. Shanks, A. C. Y. Li, L. Ateshian, J. Koch, and A. A. Houck, Imaging photon lattice states by scanning defect microscopy, *Phys. Rev. X* **6**, 021044 (2016).

[18] G.-B. Jo, J. Guzman, C. K. Thomas, P. Hosur, A. Vishwanath, and D. M. Stamper-Kurn, Ultracold atoms in a tunable optical kagome lattice, *Phys. Rev. Lett.* **108**, 045305 (2012).

[19] H. Ozawa, S. Taie, T. Ichinose, and Y. Takahashi, Interaction-driven shift and distortion of a flat band in an optical lieb lattice, *Phys. Rev. Lett.* **118**, 175301 (2017).

[20] R. A. Vicencio, C. Cantillano, L. Morales-Inostroza, B. Real, C. Mejía-Cortés, S. Weimann, A. Szameit, and M. I. Molina, Observation of localized states in lieb photonic lattices, *Phys. Rev. Lett.* **114**, 245503 (2015).

[21] S. Mukherjee, A. Spracklen, D. Choudhury, N. Goldman, P. Öhberg, E. Andersson, and R. R. Thomson, Observation of a localized flat-band state in a photonic lieb lattice, *Phys. Rev. Lett.* **114**, 245504 (2015).

[22] Y. Zong, S. Xia, L. Tang, D. Song, Y. Hu, Y. Pei, J. Su, Y. Li, and Z. Chen, Observation of localized flat-band states in kagome photonic lattices, *Opt. Express* **24**, 8877 (2016).

[23] J. Ma, J.-W. Rhim, L. Tang, S. Xia, H. Wang, X. Zheng, S. Xia, D. Song, Y. Hu, Y. Li, B.-J. Yang, D. Leykam, and Z. Chen, Direct observation of flatband loop states arising from nontrivial real-space topology, *Phys. Rev. Lett.* **124**, 183901 (2020).

[24] C. E. Whittaker, D. R. Gulevich, D. Biegańska, B. Royall, E. Clarke, M. S. Skolnick, I. A. Shelykh, and D. N. Krizhanovskii, Optical and magnetic control of orbital flat bands in a polariton lieb lattice, *Phys. Rev. A* **104**, 063505 (2021).

[25] M. M. Samak and O. R. Bilal, Direct observation of all-flat bands phononic metamaterials, *Phys. Rev. Lett.* **133**, 266101 (2024).

[26] D. Călugăru, A. Chew, L. Elcoro, Y. Xu, N. Regnault, Z.-D. Song, and B. A. Bernevig, General construction and topological classification of crystalline flat bands, *Nature Physics* **18**, 185 (2022).

[27] N. Regnault, Y. Xu, M.-R. Li, D.-S. Ma, M. Jovanovic, A. Yazdani, S. S. P. Parkin, C. Felser, L. M. Schoop,

N. P. Ong, R. J. Cava, L. Elcoro, Z.-D. Song, and B. A. Bernevig, Catalogue of flat-band stoichiometric materials, *Nature* **603**, 824 (2022).

[28] P. M. Neves, J. P. Wakefield, S. Fang, H. Nguyen, L. Ye, and J. G. Checkelsky, Crystal net catalog of model flat band materials, *npj Computational Materials* **10**, 39 (2024).

[29] H. T. Li, T. Z. Ji, R. G. Yan, W. L. Fan, Z. X. Zhang, L. Sun, B. F. Miao, G. Chen, X. G. Wan, and H. F. Ding, General method to construct flat bands in two-dimensional lattices, *Phys. Rev. Lett.* **134**, 076402 (2025).

[30] M. Sabri and P. Youssef, Flat bands of periodic graphs, *Journal of Mathematical Physics* **64**, 092101 (2023).

[31] G. Berkolaiko and P. Kuchment, *Introduction To Quantum Graphs* (AMS, 2013).

[32] E. Akkermans, A. Comtet, J. Desbois, G. Montambaux, and C. Texier, Spectral determinant on quantum graphs, *Annals of Physics* **284**, 10 (2000).

[33] L. Pauling, The diamagnetic anisotropy of aromatic molecules, *The Journal of Chemical Physics* **4**, 673 (1936).

[34] J. S. Griffith, A free-electron theory of conjugated molecules. part 1.â polycyclic hydrocarbons, *Trans. Faraday Soc.* **49**, 345 (1953).

[35] C. A. Coulson, Note on the applicability of the free-electron network model to metals, *Proceedings of the Physical Society. Section A* **67**, 608 (1954).

[36] K. Kazymyrenko and B. Douçot, Regular networks of luttinger liquids, *Phys. Rev. B* **71**, 075110 (2005).

[37] P. G. de Gennes, —, *Comptes Rendus de l'Académie des Sciences, Série B* **292**, 279 (1981).

[38] H. J. Fink, A. López, and R. Maynard, Magnetic phase boundary of simple superconductive micronetworks, *Phys. Rev. B* **26**, 5237 (1982).

[39] S. Alexander, Superconductivity of networks. a percolation approach to the effects of disorder, *Phys. Rev. B* **27**, 1541 (1983).

[40] R. Rammal, T. C. Lubensky, and G. Toulouse, Superconducting networks in a magnetic field, *Phys. Rev. B* **27**, 2820 (1983).

[41] J. T. Chalker and P. D. Coddington, Percolation, quantum tunnelling and the integer hall effect, *Journal of Physics C: Solid State Physics* **21**, 2665 (1988).

[42] T. Kottos and U. Smilansky, Quantum chaos on graphs, *Phys. Rev. Lett.* **79**, 4794 (1997).

[43] T. Kottos and U. Smilansky, Periodic orbit theory and spectral statistics for quantum graphs, *Annals of Physics* **274**, 76 (1999).

[44] T. Kottos and U. Smilansky, Chaotic scattering on graphs, *Phys. Rev. Lett.* **85**, 968 (2000).

[45] N. Anantharaman, M. Ingremeau, M. Sabri, and B. Winn, Quantum ergodicity for expanding quantum graphs in the regime of spectral delocalization, *Journal de Mathématiques Pures et Appliquées* **151**, 28 (2021).

[46] S. N. Kempkes, M. R. Slot, S. E. Freeney, S. J. M. Zevenhuizen, D. Vanmaekelbergh, I. Swart, and C. M. Smith, Design and characterization of electrons in a fractal geometry, *Nature Physics* **15**, 127 (2019).

[47] D. Bercioux and A. Iñiguez, Quantum fractals, *Nature Physics* **15**, 111 (2019).

[48] P. Kuchment and O. Post, On the spectra of carbon nanostructures, *Communications in Mathematical Physics* **275**, 805 (2007).

[49] C. R. de Oliveira and V. L. Rocha, Bidimensional honeycomb materials: A graph model through dirac operator, *Reports on Mathematical Physics* **89**, 231 (2022).

[50] D. K. Efimkin and A. H. MacDonald, Helical network model for twisted bilayer graphene, *Phys. Rev. B* **98**, 035404 (2018).

[51] H. K. Pal, S. Spitz, and M. Kindermann, Emergent geometric frustration and flat band in moiré bilayer graphene, *Phys. Rev. Lett.* **123**, 186402 (2019).

[52] C. De Beule, V. o. T. Phong, and E. J. Mele, Network model for periodically strained graphene, *Phys. Rev. B* **107**, 045405 (2023).

[53] H. J. W. Zandvliet, P. Bampoulis, C. M. Smith, and L. Eek, Electric field-induced spin-valley locking in twisted bilayer buckled honeycomb materials (2025), arXiv:2510.14404 [cond-mat.mes-hall].

[54] C. Naud, G. Faini, and D. Mailly, Aharonov-bohm cages in 2d normal metal networks, *Phys. Rev. Lett.* **86**, 5104 (2001).

[55] F. Schopfer, F. m. c. Mallet, D. Mailly, C. Texier, G. Montambaux, C. Bäuerle, and L. Saminadayar, Dimensional crossover in quantum networks: From macroscopic to mesoscopic physics, *Phys. Rev. Lett.* **98**, 026807 (2007).

[56] C. Wu, D. Bergman, L. Balents, and S. Das Sarma, Flat bands and wigner crystallization in the honeycomb optical lattice, *Phys. Rev. Lett.* **99**, 070401 (2007).

[57] C. Wu and S. Das Sarma, $p_{x,y}$ -orbital counterpart of graphene: Cold atoms in the honeycomb optical lattice, *Phys. Rev. B* **77**, 235107 (2008).

[58] R. Bistritzer and A. H. MacDonald, Moiré bands in twisted double-layer graphene, *Proceedings of the National Academy of Sciences* **108**, 12233 (2011).

[59] See Supplemental Material for further details about the single channel HQG, the scattering matrices and FBs in the multichannel HQG, and the 2D antidot model.

[60] Explicitly S_v consists in repeated identical reflection amplitude r_v on its diagonal, and a unique transmission amplitude t_v on non-diagonal entries. The complex transmission and reflection amplitudes are given respectively by $t_v = (e^{i\theta_v} - e^{i\phi_v})/3$ and $r_v = (e^{i\theta_v} + 2e^{i\phi_v})/3$ as a function of the angular parameters (θ_v, ϕ_v) .

[61] M. Ezawa, Higher-order topological insulators and semimetals on the breathing kagome and pyrochlore lattices, *Phys. Rev. Lett.* **120**, 026801 (2018).

[62] A. Bolens and N. Nagaosa, Topological states on the breathing kagome lattice, *Phys. Rev. B* **99**, 165141 (2019).

[63] D. L. Bergman, C. Wu, and L. Balents, Band touching from real-space topology in frustrated hopping models, *Phys. Rev. B* **78**, 125104 (2008).

[64] J.-W. Rhim and B.-J. Yang, Classification of flat bands according to the band-crossing singularity of bloch wave functions, *Phys. Rev. B* **99**, 045107 (2019).

[65] Y. Hwang, J.-W. Rhim, and B.-J. Yang, General construction of flat bands with and without band crossings based on wave function singularity, *Phys. Rev. B* **104**, 085144 (2021).

[66] A. Graf and F. Piéchon, Designing flat-band tight-binding models with tunable multifold band touching points, *Phys. Rev. B* **104**, 195128 (2021).

[67] M. R. Slot, T. S. Gardenier, P. H. Jacobse, G. C. P. van Miert, S. N. Kempkes, S. J. M. Zevenhuizen, C. M. Smith, D. Vanmaekelbergh, and I. Swart, Experimental realization and characterization of an electronic lieb lattice, *Nature Physics* **13**, 672 (2017).

[68] Y. Cao, V. Fatemi, S. Fang, K. Watanabe, T. Taniguchi, E. Kaxiras, and P. Jarillo-Herrero, Unconventional su-

perconductivity in magic-angle graphene superlattices, *Nature* **556**, 43 (2018).

[69] H. Zhou, T. Xie, T. Taniguchi, K. Watanabe, and A. F. Young, Superconductivity in rhombohedral trilayer graphene, *Nature* **598**, 434 (2021).

[70] B. R. Ortiz, S. M. L. Teicher, Y. Hu, J. L. Zuo, P. M. Sarte, E. C. Schueller, A. M. M. Abeykoon, M. J. Krogstad, S. Rosenkranz, R. Osborn, R. Seshadri, L. Balents, J. He, and S. D. Wilson, Cs_3Sb_5 : A \mathbb{Z}_2 topological kagome metal with a superconducting ground state, *Physical Review Letters* **125**, 247002 (2020).

[71] This construction applies to any “homogeneous” lattices, namely lattice graphs that are regular, and transforms transitively under the lattice symmetry group.

A. Details of the single channel HQG

1. Bloch reduction and secular equation

Each point is parameterized by a set of coordinates (m, n, i, x) , where $\mathbf{l} = (m, n, i)$ specifies the bond, $i = 1, 2, 3$ the direction, and x the local linear coordinate along the bond $\mathbf{l} = (m, n, i)$, with convention $x = 0$ at site B and $x = a_0$ at site A .

We have

$$\begin{pmatrix} e^{-iqa_0} \beta_1^{m,n} \\ e^{-iqa_0} \beta_2^{m,n} \\ e^{-iqa_0} \beta_3^{m,n} \end{pmatrix} = S_A \begin{pmatrix} e^{iqa_0} \alpha_1^{m,n} \\ e^{iqa_0} \alpha_2^{m,n} \\ e^{iqa_0} \alpha_3^{m,n} \end{pmatrix}, \quad \begin{pmatrix} \alpha_1^{m,n} \\ \alpha_2^{m-1,n} \\ \alpha_3^{m,n-1} \end{pmatrix} = S_B \begin{pmatrix} \beta_1^{m,n} \\ \beta_2^{m-1,n} \\ \beta_3^{m,n-1} \end{pmatrix}. \quad (\text{A1})$$

Bloch theorem states that

$$\psi(m, n, i, x) = e^{i\mathbf{k}\cdot(\mathbf{e}_1+\mathbf{e}_2)} \psi(0, 0, i, x),$$

giving

$$\alpha_i^{m,n} = e^{i\mathbf{k}\cdot(m\mathbf{e}_1+n\mathbf{e}_2)} \alpha_i^{0,0}, \quad \beta_i^{m,n} = e^{i\mathbf{k}\cdot(m\mathbf{e}_1+n\mathbf{e}_2)} \beta_i^{0,0},$$

So

$$\begin{pmatrix} \beta_1^{0,0} \\ \beta_2^{0,0} \\ \beta_3^{0,0} \end{pmatrix} = S_A e^{2iqa_0} \begin{pmatrix} \alpha_1^{0,0} \\ \alpha_2^{0,0} \\ \alpha_3^{0,0} \end{pmatrix}, \quad \begin{pmatrix} \alpha_1^{0,0} \\ e^{-i\mathbf{k}\cdot\mathbf{e}_1} \alpha_2^{0,0} \\ e^{-i\mathbf{k}\cdot\mathbf{e}_2} \alpha_3^{0,0} \end{pmatrix} = S_B \begin{pmatrix} \beta_1^{0,0} \\ e^{-i\mathbf{k}\cdot\mathbf{e}_1} \beta_2^{0,0} \\ e^{-i\mathbf{k}\cdot\mathbf{e}_2} \beta_3^{0,0} \end{pmatrix}. \quad (\text{A2})$$

Define $\mathbf{a} = (\alpha_1^{0,0}, \alpha_2^{0,0}, \alpha_3^{0,0}, \beta_1^{0,0}, \beta_2^{0,0}, \beta_3^{0,0})^T$, We have

$$S(\mathbf{k}, q)\mathbf{a} = \mathbf{a},$$

where

$$S(\mathbf{k}, q) = \begin{pmatrix} 0 & D_{\mathbf{k}}^{\dagger} S_B D_{\mathbf{k}} \\ S_A e^{2iqa_0} & 0 \end{pmatrix}, \quad (\text{A3})$$

with

$$D_{\mathbf{k}} = \text{Diag}(1, e^{-i\mathbf{k}\cdot\mathbf{e}_1}, e^{-i\mathbf{k}\cdot\mathbf{e}_2}). \quad (\text{A4})$$

2. Dispersive bands

We discuss here the structure of the dispersive bands in the single channel case, to complement our study of the flat bands. The band structure consists in the periodic repetition (for the variable q) of a group of 3 bands, comprising the flat band discussed previously, and two bands that have a dispersion (in the generic cases) as function of \mathbf{k} . The two (generically) dispersive bands satisfy the following trigonometric equation

$$\cos(2q + \alpha_{++}^{++}) = \frac{2}{9} f(\mathbf{k}) (\cos \alpha_{--}^{++} - \cos \alpha_{-+}^{+-}) + \frac{1}{3} \cos \alpha_{--}^{++} + \frac{2}{3} \cos \alpha_{-+}^{+-}, \quad (\text{A5})$$

where we defined

$$f(\mathbf{k}) = \sum_{i=0}^2 \cos(\mathbf{k} \cdot \mathbf{e}_i), \quad (\text{A6})$$

with $\mathbf{e}_0 = \mathbf{e}_1 - \mathbf{e}_2$. We have also introduced the linear combinations of scattering phases :

$$\alpha_{s_3, s_4}^{s_1, s_2} = \frac{1}{2}(s_1\theta_A + s_2\theta_B + s_3\phi_A + s_4\phi_B), \quad (\text{A7})$$

where $s_i = \pm 1$ for $i = 1, 2, 3, 4$. The full spectrum consists in a group of three bands (one flat + two dispersive) which is repeated periodically in q . The dispersive bands can be tuned *without altering* the flat bands. The condition for all bands being flat is easily seen from Eq. (A5): $\cos \alpha_{-+}^{++} = \cos \alpha_{-+}^{+-}$.

We observe that for certain values of parameters $(\theta_A, \theta_B, \phi_A, \phi_B)$, Dirac points exist at the Bloch momentum $K = \left(\frac{2\pi}{3\sqrt{3}a_0}, \frac{2\pi}{3a_0}\right)$. To see this, expand the dispersion (A5) around K : $\mathbf{k} \rightarrow K + \mathbf{k}$, we have

$$\pm \sin(\alpha_{-+}^{+-})(k - E_{\pm}) + \cos(\alpha_{-+}^{+-})(k - E_{\pm})^2 + o((k + E_{-})^3) = \frac{1}{4}|\mathbf{k}|^2 \sin \frac{\theta_A - \phi_A}{2} \sin \frac{\theta_B - \phi_B}{2}, \quad (\text{A8})$$

where we defined $E_+ := -\frac{1}{2}(\theta_B + \phi_A)$ and $E_- := -\frac{1}{2}(\theta_A + \phi_B)$. We see that a Dirac dispersion appears whenever $\alpha_{-+}^{+-} = 0 \pmod{\pi}$: in this case $q = E_{\pm} \pm \frac{1}{2}|\mathbf{k}|$, and $E = q^2 \sim E_{\pm}^2 \pm E_{\pm}|\mathbf{k}| + o(|\mathbf{k}|^2)$.

3. Berry curvature of the lowest flat band

In this section we assume that we are away from the Γ point in the Brillouin zone, where the FB touches the dispersive band and Berry curvature is ill-defined.

When $\mathbf{k} \neq 0$, the normalized eigenvector $|\alpha_{\mathbf{k}}\rangle$ corresponding to the flat band has the expression

$$|\alpha_{\mathbf{k}}\rangle = \frac{(e^{i\mathbf{k} \cdot \mathbf{e}_1} - e^{i\mathbf{k} \cdot \mathbf{e}_2}, e^{i\mathbf{k} \cdot \mathbf{e}_2} - 1, 1 - e^{i\mathbf{k} \cdot \mathbf{e}_1})}{\sqrt{|e^{i\mathbf{k} \cdot \mathbf{e}_1} - e^{i\mathbf{k} \cdot \mathbf{e}_2}|^2 + |e^{i\mathbf{k} \cdot \mathbf{e}_2} - 1|^2 + |1 - e^{i\mathbf{k} \cdot \mathbf{e}_1}|^2}} \quad (\text{A9})$$

and we have $|\beta_{\mathbf{k}}\rangle = e^{2iqa_0} S_A |\alpha_{\mathbf{k}}\rangle$ where S_A is independent of \mathbf{k} , so that $|\alpha_{\mathbf{k}}\rangle$ and $|\beta_{\mathbf{k}}\rangle$ contributes identically to Berry curvature $\mathcal{F}(\mathbf{k})$. We have

$$\begin{aligned} \mathcal{F}(\mathbf{k}) &= i\epsilon^{ij}(\partial_{k_i} \langle \alpha_{\mathbf{k}} |)^\dagger (\partial_{k_j} | \alpha_{\mathbf{k}} \rangle) \\ &= -\frac{9\sqrt{3} \sin \frac{\sqrt{3}k_x}{2} \left(\cos \frac{\sqrt{3}k_x}{2} - \cos \frac{3k_y}{2} \right)}{2 \left(2 \cos \frac{\sqrt{3}k_x}{2} \cos \frac{3k_y}{2} + \cos(\sqrt{3}k_x) - 3 \right)^2}, \end{aligned} \quad (\text{A10})$$

which is well-behaved in the Brillouin zone except at the Γ point, where $\mathcal{F}(\mathbf{k})$ can be expanded to

$$\mathcal{F}(\mathbf{k}) = \cos(3\theta) \left(\frac{1}{2k} + \frac{3}{32}k \right) + O(k^3), \quad (\text{A11})$$

where $k = |\mathbf{k}|$ and $\theta = \arg(k_x + ik_y)$. We see that the area integral of the Berry curvature vanishes on disks centered at Γ with arbitrary small radius.

4. Compact localized states

The energies of the various FBs are obtained by the formula

$$2q + \phi_A + \phi_B = 2\pi p, \quad q > 0, \quad (\text{A12})$$

with the prescription $q > 0$, and then $E = q^2$. The wave function Eq. (7) reads :

$$\Psi(s) = 2\alpha e^{-i\phi_B/2} \cos \left(qs + \frac{\phi_B}{2} \right) = 2\beta e^{i\phi_B/2} \cos \left(qs + \frac{\phi_B}{2} \right). \quad (\text{A13})$$

The condition to have a node at the B site is $\Psi(0) = 0$, hence $\phi_B = \pm\pi$. Similarly the condition to have a node at the A site is $\Psi(1) = 0$, hence $\phi_A = \pm\pi$. Enforcing a node at both A and B vertices leads to the Neumann-Dirichlet case.

Now let us investigate the condition for observing a node at local coordinate $0 < s < 1$ strictly located at the interior of a bond :

$$qs + \frac{\phi_b}{2} = \frac{\pi}{2} + l\pi \quad (\text{A14})$$

Because $q > 0$ and $0 < s < 1$:

$$0 < qs < q = \pi p - \frac{\phi_A + \phi_b}{2} \quad (\text{A15})$$

The integer l has therefore to satisfy the inequalities :

$$\frac{\phi_B}{2} - \frac{\pi}{2} < \pi l < \pi(p - \frac{1}{2}) - \frac{\phi_A}{2} \quad (\text{A16})$$

We consider $(\phi_A, \phi_B) \in]-\pi, \pi[^2$. The minimal value for l is then $l = 0$, and its maximal value is $l = p - 1$. Therefore, the number of nodes along each bond is equal to p , it increases by one upon going from one flat band to the next one higher up in energy. In particular, it is equal to zero when $p = 0$. This can happen only when $\phi_A + \phi_B < 0$. When $\phi_A + \phi_B > 0$, the minimal value of p is $p = 1$. The difference between these two cases is illustrated on Fig. 2, where p is assumed to take its minimal value, depending on the sign of $\phi_A + \phi_B$.

B. Group theory derivation on the multichannel case

Here we present a detailed derivation of the multichannel S matrix for the 2D honeycomb and 3D diamond lattices [71]. Quite generally, we denote Z as the degree of (any) vertex, N_+ (N_-) the number of parity-even (parity-odd) channels on each edge, $N = N_+ + N_-$ the total number of channels on each edge, and G the onsite symmetry group of the vertex. Then the ZN channels form a tensor product of two representations of the group G

$$\mathbb{C}^N \otimes \mathbb{C}^Z \cong (\mathbf{1}_+^{\otimes N_+} \oplus \mathbf{1}_-^{\otimes N_-}) \otimes \mathbf{Perm}, \quad (\text{B1})$$

where **Perm** denotes the Z -dimensional representation formed by the edge basis $|x\rangle$, $x = 1, 2, \dots, Z$, on which all point group operation acts as certain permutation of those edges. The **Perm** representation is generally reducible, as the vector $|e_Z\rangle = (1, \dots, 1)^T / \sqrt{Z}$ is obviously an invariant one-dimensional subspace of G . The task is then to first decompose the Z -dimensional **Perm** into irreps, and then the ZN -dimensional representation $\mathbb{C}^N \otimes \mathbb{C}^Z$ into irreps; this gives the most general parameterization of the S matrix allowed by the symmetry G .

1. 2D Honeycomb

The 2D honeycomb network has a site symmetry group of D_3 , generated by a threefold rotation C_3 and a mirror reflection M . (The order-2 element M can be equivalently interpreted as a twofold rotation C'_2 whose axis lies in the plane – These interpretations do not alter any analysis below.) The degree of vertex is $Z = 3$. The permutation representation $\mathbb{C}^3 = \mathbf{Perm}$ is defined in the basis of three edges $|x\rangle$, $x = 1, 2, 3$, that are permuted by D_3 according to

$$O_{C_3} = \begin{pmatrix} 0 & 1 & 0 \\ 0 & 0 & 1 \\ 1 & 0 & 0 \end{pmatrix}, \quad O_M = \begin{pmatrix} 0 & 1 & 0 \\ 1 & 0 & 0 \\ 0 & 0 & 1 \end{pmatrix}. \quad (\text{B2})$$

We have

$$\mathbf{Perm} = \mathbf{1}_+ \oplus \mathbf{2}, \quad (\text{B3})$$

where the trivial representation $\mathbf{1}_+$ is the invariant subspace $|e\rangle = \frac{1}{\sqrt{3}}(1, 1, 1)^T$. Plugging Eq. (B3) to Eq. (B1) (for $Z = 3$), we get

$$\mathbb{C}^N \otimes \mathbb{C}^3 = \mathbf{1}_+^{\otimes N_+} \oplus \mathbf{1}_-^{\otimes N_-} \oplus \mathbf{2}^{\otimes N}, \quad (\text{B4})$$

where we used the following facts: $\mathbf{1}_+ \otimes R = R$ for any representation R , and $\mathbf{1}_- \otimes \mathbf{2} = \mathbf{2}$. This shows that the $3N$ channels decompose to N_+ copies of the trivial irrep $\mathbf{1}_+$ of D_3 , N_- copies of the sign irrep $\mathbf{1}_-$ of D_3 , and N copies of the 2D irrep $\mathbf{2}$ of D_3 .

To obtain a concrete decomposition of $\mathbb{C}^N \otimes \mathbb{C}^3$ into irreducible subspaces, we use the projector formula: for any irrep λ of a group G , the projector onto the irrep λ (with multiplicities) is

$$P_\lambda = \frac{d_\lambda}{|G|} \sum_{g \in G} \chi_\lambda^*(g) U_g, \quad (\text{B5})$$

where d_λ is the dimension of the irrep, U_g is the representation matrix associated to the group element g , and $\chi_\lambda(g)$ is the character of the irrep λ . For us, concretely, we have

$$U_{C_3} = \mathbb{I}_N \otimes O_{C_3}, \quad U_M = \text{diag}(\mathbb{I}_{N_+}, -\mathbb{I}_{N_-}) \otimes O_M, \quad (\text{B6})$$

and the representation matrices for other group elements can be generated from them. Then, plugging these matrices into Eq. (B5) gives

$$P_{\mathbf{1}_+} = P_+ \otimes P, \quad P_{\mathbf{1}_-} = P_- \otimes P, \quad P_{\mathbf{2}} = \mathbb{I}_N \otimes (2 \cdot \mathbb{I}_3 - O_{C_3} - O_{C_3}^2), \quad (\text{B7})$$

which give a decomposition of identity $\mathbb{I}_{3N} = P_+ \otimes P + P_- \otimes P + \mathbb{I}_N \otimes (\mathbb{I}_3 - P)$.

To obtain a concrete parametrization of the scattering matrix S , notice that within each sector of irreducible subspaces with multiplicity, the degenerate subspaces can freely rotate among them. The subspaces of $\mathbf{1}_+$, $\mathbf{1}_-$, and $\mathbf{2}$ have degeneracies N_+ , N_- , and N , respectively, and the rotations are characterized by

$$Y_+ \in U(N_+), \quad Y_- \in U(N_-), \quad X \in U(N). \quad (\text{B8})$$

The S matrix is the intertwiner of the representation (B4), namely it commutes with the symmetry action: $[S, U_{C_3}] = [S, U_M] = 0$. By Schur's lemma, the S matrix does not mix different irreps, so in the basis of the last line of Eq. (B4) it assumes the form of a block diagonal matrix. In the original basis, \mathbb{C}^{3N} , the S matrix is obtained by replacing the projectors — which acts as identity in each degenerate subspace — with the rotation matrix in Eq. (B8). Given the form of the projectors, this can be easily achieved

$$P_+ \otimes P \rightarrow \text{diag}(Y_+, 0) \otimes P, \quad P_- \otimes P \rightarrow \text{diag}(0, Y_-) \otimes P, \quad \mathbb{I}_N \otimes (\mathbb{I}_3 - P) \rightarrow X \otimes (\mathbb{I}_3 - P), \quad (\text{B9})$$

and this gives Eq. (8) in the main text.

2. 3D Diamond

The 3D honeycomb network has a site symmetry group T_d , generated by a threefold rotation C_3 and a mirror reflection M . The degree of vertex is $Z = 4$. The permutation representation $\mathbb{C}^4 = \mathbf{Perm}$ is defined in the basis of the four edges $|x\rangle$, $x = 1, 2, 3, 4$, that are permuted by T_d according to

$$O_{C_3} = \begin{pmatrix} 1 & 0 & 0 & 0 \\ 0 & 0 & 1 & 0 \\ 0 & 0 & 0 & 1 \\ 0 & 1 & 0 & 0 \end{pmatrix}, \quad O_M = \begin{pmatrix} 0 & 1 & 0 & 0 \\ 1 & 0 & 0 & 0 \\ 0 & 0 & 1 & 0 \\ 0 & 0 & 0 & 1 \end{pmatrix} \quad (\text{B10})$$

We have

$$\mathbf{Perm} = \mathbf{1}_+ \oplus \mathbf{3}_-, \quad (\text{B11})$$

where the trivial representation $\mathbf{1}_+$ is the invariant subspace $|e_4\rangle = \frac{1}{\sqrt{4}}(1, 1, 1, 1)^T$; the 3D irrep $\mathbf{3}_-$ is conventionally labeled as T_2 in crystallography. Plugging Eq. (B11) to Eq. (B1), we get

$$\mathbb{C}^N \otimes \mathbb{C}^4 = \mathbf{1}_+^{\otimes N_+} \oplus \mathbf{1}_-^{\otimes N_-} \oplus \mathbf{3}_-^{\otimes N_+} \oplus \mathbf{3}_+^{\otimes N_-}, \quad (\text{B12})$$

where we used the fact $\mathbf{1}_- \otimes \mathbf{3}_- = \mathbf{3}_+$. This shows that the $4N$ channels decompose to N_+ copies of the irreps $\mathbf{1}_+$ and $\mathbf{3}_-$, and N_- copies of the irreps $\mathbf{1}_-$ and $\mathbf{3}_+$. Following the calculation in the 2D honeycomb case around Eq. (B5), we have the parameterization of the S matrix for any diamond vertex

$$S = \text{diag}(X_+, X_-) \otimes P_4 + \text{diag}(Y_+, Y_-) \otimes (\mathbb{I}_4 - P_4), \quad (\text{B13})$$

where $P_4 = |e_4\rangle\langle e_4|$, $X_+, Y_+ \in U(N_+)$ and $X_-, Y_- \in U(N_-)$ are arbitrary matrices in the corresponding unitary group.

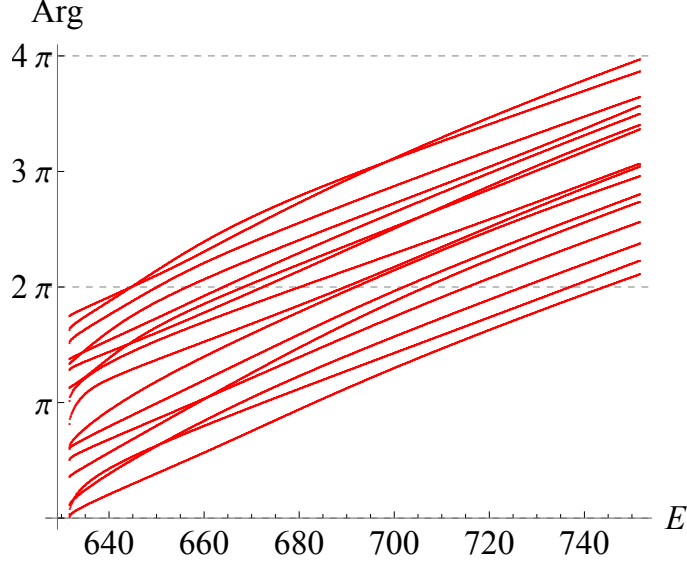


Figure 5. The argument of the eigenvalues of $e^{iQ(E)} S_{B,0} e^{iQ(E)} S_{A,0}$ as a function of E : we choose arbitrary $S_{A/B,0} \in U(N)$ with $N = N_p + N_n = 16$, and $w = 2$. Whenever one of the arguments reaches multiples of 2π (shown as horizontal dashed gray line) an eigenvalue of $\lambda = 1$ is resulted.

C. Proof for the existence of flat bands in the multichannel case

Here we show one of the main results of this work, namely that flat bands persist in the multichannel case. We use the tensor decomposition of the S_v matrices given by Eq. (8) :

$$S_v = S_{v,0} \otimes P_{\perp} + \text{diag}(S_{v,+}, S_{v,-}) \otimes P_{\parallel}, \quad (\text{C1})$$

and a generalization of the type of linear algebra argument already presented for the single channel case in the main text. To this purpose, we look for eigenvectors $|\phi\rangle \otimes |\chi_{\mathbf{k}}\rangle$ that solve the following eigenproblem with eigenvalue one :

$$(e^{iQ(E)} \otimes D_{\mathbf{k}}^{\dagger}) S_B (e^{iQ(E)} \otimes D_{\mathbf{k}}) S_A [|\phi\rangle \otimes |\chi_{\mathbf{k}}\rangle] = |\phi\rangle \otimes |\chi_{\mathbf{k}}\rangle, \quad (\text{C2})$$

such that $Q(E)$ does not depends on Bloch momentum \mathbf{k} . The difficulty is that $D_{\mathbf{k}}$ and $D_{\mathbf{k}}^{\dagger}$ does depend on \mathbf{k} and do not commute with the projectors P_{\perp} and P_{\parallel} involved in the scattering matrices S_v with $v = A, B$, unless for $\mathbf{k} = 0$.

As in the single channel case, the main idea is to choose a class of states such that $|\chi_{\mathbf{k}}\rangle \in \text{Im}P_{\perp}$ and $D_{\mathbf{k}}^{\dagger}|\chi_{\mathbf{k}}\rangle \in \text{Im}P_{\perp}$. For such states, it is easy to compute the action of such chain of matrices. First, we start by acting on the ket as :

$$(e^{iQ(E)} \otimes D_{\mathbf{k}}) S_A [|\phi\rangle \otimes |\chi_{\mathbf{k}}\rangle] = e^{iQ(E)} S_{A,0} |\phi\rangle \otimes D_{\mathbf{k}} |\chi_{\mathbf{k}}\rangle, \quad (\text{C3})$$

Then we apply the action of rest of the matrix chain to obtain :

$$(e^{iQ(E)} \otimes D_{\mathbf{k}}^{\dagger}) S_B [e^{iQ(E)} S_{A,0} |\phi\rangle \otimes D_{\mathbf{k}} |\chi_{\mathbf{k}}\rangle] = e^{iQ(E)} S_{B,0} e^{iQ(E)} S_{A,0} |\phi\rangle \otimes D_{\mathbf{k}}^{\dagger} D_{\mathbf{k}} |\chi_{\mathbf{k}}\rangle, \quad (\text{C4})$$

So finally the eigenvalue problem reduces to, for the class of states we have selected :

$$e^{iQ(E)} S_{B,0} e^{iQ(E)} S_{A,0} |\phi\rangle \otimes |\chi_{\mathbf{k}}\rangle = |\phi\rangle \otimes |\chi_{\mathbf{k}}\rangle, \quad (\text{C5})$$

since $D_{\mathbf{k}}^{\dagger} D_{\mathbf{k}} = \mathbb{I}_3$. Therefore we need to find energy E and vector $|\phi\rangle \in \mathbb{C}^N$ such that :

$$e^{iQ(E)} S_{B,0} e^{iQ(E)} S_{A,0} |\phi\rangle = |\phi\rangle$$

(C6)

The matrix $e^{iQ(E)} S_{B,0} e^{iQ(E)} S_{A,0}$ belongs to $U(N)$ (acting within the space of transverse channels) and its N possible unimodular eigenvalues $\lambda_i(E)$ can be represented on the unit circle. Each time, one of those eigenvalue $\lambda_i(E)$ hits the value 1 (or its phase hits multiples of 2π), then E is the energy for a flat band. The phase of the eigenvalues as a function of E is shown in Fig. 5.

Below we show that at least one eigenvalue $\lambda_i(E)$ hits the value 1 upon increasing E . The condition (C6) is equivalent to the following condition

$$\exists E \quad \text{s.t.} \quad \det(e^{iQ(E)} S_{B,0} e^{iQ(E)} S_{A,0} - \mathbb{I}_N) = 0. \quad (\text{C7})$$

We will first provide an algebraic proof for the $N = 2$ case (this is the “smallest” multi-channel case), and then present a proof for the general N case; the proof applies to any functions $q_j(E)$ that are unbounded and increasing for all j .

1. $N = 2$: an algebraic proof

In the case of $N = 2$, we introduce the parametrization for the $U(2)$ matrix

$$e^{i\alpha} e^{i\psi \mathbf{n} \cdot \boldsymbol{\sigma}} := e^{iQ(E)} S_{B,0} e^{iQ(E)} S_{A,0} \in U(2) \quad (\text{C8})$$

where $\alpha(E) = q_1(E) + q_2(E) + \alpha_A + \alpha_B$ with $\alpha_{A/B} := \text{Im} \log \det(S_{A/B,0})$. The detailed expressions of ψ and \mathbf{n} do not concern us. The parametrization (C8) then simplifies Eq. (C7) to

$$\cos(\alpha(E)) = \cos(\psi(E)), \quad \text{for some } E. \quad (\text{C9})$$

As $\alpha(E)$ is a strictly increasing and unbounded (continuous) function of E , $\cos(\alpha(E))$ maps surjectively onto $[-1, 1]$, and there must be some E satisfying Eq. (C9) regardless of the functional dependence of $\psi(E)$. This proves the existence of flat bands in the special case of $N = 2$.

2. A topological argument for arbitrary N and any unbounded function $q_\mu(E)$

To prove the statement (C7) in the general N case, we study

$$f(z) = \text{Im} \log \det(e^{iQ(z)} S_{B,0} e^{iQ(z)} S_{A,0}) \quad (\text{C10})$$

as a map $\mathbb{C} \rightarrow \mathbb{R}$. Note that this function is *unbounded* on the real axis, as $\lim_{E \rightarrow \infty} q_\mu(E) \rightarrow \infty$.

We prove (C7) by contradiction: assume that

$$\det(e^{iQ(E)} S_{B,0} e^{iQ(E)} S_{A,0} - \mathbb{I}_N) \neq 0 \text{ for any } E \in [(\pi N/w)^2, \infty) \quad (\text{C11})$$

then we have (a proof is provided shortly):

$$\text{Any eigenvalue } \lambda_\mu(z) := e^{i\vartheta_\mu(z)} \text{ of } e^{iQ(z)} S_{B,0} e^{iQ(z)} S_{A,0} \text{ contributes a finite phase } \vartheta_\mu(z) \in [-\pi, \pi] \text{ to } f(z). \quad (\text{C12})$$

but this implies that $f(z) = \sum_{\mu=1}^N \vartheta_\mu(z) \in [-N\pi, N\pi]$ is bounded, contradicting the unboundedness of $f(z)$ on $z = E \in [(\pi N/w)^2, \infty)$. This shows that the assumption (C11) is incorrect, proving (C7).

Below we provide a technical proof for the statement (C12). $\det(e^{iQ(E)} S_{B,0} e^{iQ(E)} S_{A,0} - \mathbb{I}_N) \neq 0$ implies that the following Cayley transform is well-defined:

$$H(z) = i \frac{\mathbb{I}_N + e^{iQ(z)} S_{B,0} e^{iQ(z)} S_{A,0}}{\mathbb{I}_N - e^{iQ(z)} S_{B,0} e^{iQ(z)} S_{A,0}}, \quad (\text{C13})$$

and the phase $\vartheta_\mu(z)$ is related to the eigenvalue $h_\mu(z)$ of $H(z)$ by

$$\vartheta_\mu = \arg \left(\frac{\lambda_\mu - i}{\lambda_\mu + i} \right) = -2 \arctan(1/h_\mu) \in (-\pi, \pi), \quad (\text{C14})$$

proving (C12).

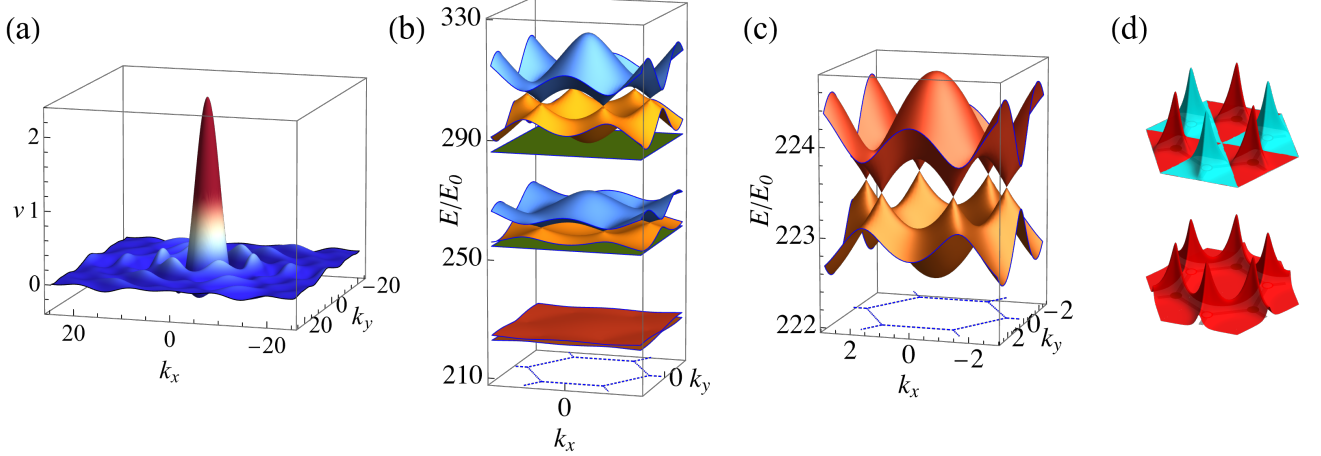


Figure 6. Various plots for the flat band regime $(V_0/E_0, w/a_0) = (400, \sqrt{3}/20)$. (a) the function $v(\mathbf{k}, 0.95)$ (see Eq. (D4)) obtained from the Fourier transform of $V(\mathbf{r})$; the color shows the height. (b) Low energy bands on the Brillouin zone (blue dashed hexagon); the (approximately) flat bands are shown in green. (c) Zoom-in view of the lowest two bands in (b). (d) Wave functions of the bound states corresponding to the Γ point (center of the Brillouin zone) of the two bands in (c).

D. Crossover between 2DEG and 1D HQG

1. Derivation

Here we derive a matrix representation of the 2DEG problem of periodic triangular array of hexagonal antidots considered in the main text. The matrix representation is amenable to numerically access the spectrum and eigenstates, which we show in the next subsection.

As the potential $V(\mathbf{r})$ is periodic, we apply Bloch theorem to write $\psi(\mathbf{r}) = e^{i\mathbf{k}\cdot\mathbf{r}}u_{\mathbf{k}}(\mathbf{r})$ where \mathbf{k} is the Bloch quasi-momentum, and $u_{\mathbf{k}}(\mathbf{r})$ is periodic, namely $u_{\mathbf{k}}(\mathbf{r} + \mathbf{e}_i) = u_{\mathbf{k}}(\mathbf{r})$ for $i = 1, 2$. We need to solve

$$((-i\nabla + \mathbf{k})^2 + V(\mathbf{r}))u_{\mathbf{k}}(\mathbf{r}) = E(\mathbf{k})u_{\mathbf{k}}(\mathbf{r}). \quad (\text{D1})$$

This problem can be solved in the plane wave basis. When $V_0 = 0$, we have the solution

$$u_{\mathbf{k}}^{m,n}(\mathbf{r}) = \frac{1}{\sqrt{A}}e^{i(m\mathbf{b}_1 + n\mathbf{b}_2)\cdot\mathbf{r}}, \quad E_0^{m,n}(\mathbf{k}) = (m\mathbf{b}_1 + n\mathbf{b}_2 + \mathbf{k})^2, \quad (\text{D2})$$

where $A = \frac{3\sqrt{3}}{2}a_0^2$ is the area of the unit cell. We calculate the matrix elements for the potential $V(\mathbf{r})$ in the basis of $u_{\mathbf{k}}^{m,n}$:

$$\begin{aligned} V_{m,n;m',n'} &= V_0 \int_{\mathbf{Hex}} \int_{\mathbf{Hex}} (u_{\mathbf{k}}^{m,n}(\mathbf{r}))^* u_{\mathbf{k}}^{m',n'}(\mathbf{r}') d\mathbf{r} d\mathbf{r}' \\ &= \frac{V_0}{A} \int_{\bigoplus_{(m,n), 1-w/\sqrt{3}}} e^{-i((m-m')\mathbf{b}_1 + (n-n')\mathbf{b}_2)\cdot\mathbf{r}} d\mathbf{r} \\ &= \frac{V_0}{A} v \left((m-m')\mathbf{b}_1 + (n-n')\mathbf{b}_2, 1 - w/\sqrt{3} \right), \end{aligned} \quad (\text{D3})$$

where we abbreviated $\mathbf{Hex} = \bigcup_{m,n \in \mathbb{Z}} \bigoplus_{(m,n), 1-w/\sqrt{3}}$, and

$$v(\mathbf{k}, r) \equiv \frac{4\sqrt{3}k_y \left(\cos(k_y r) - \cos\left(\frac{\sqrt{3}}{2}k_x r\right) \cos\frac{k_y r}{2} \right) + 12k_x \sin\left(\frac{\sqrt{3}}{2}k_x r\right) \sin\frac{k_y r}{2}}{(3k_x^2 - k_y^2)k_y}. \quad (\text{D4})$$

the \mathbf{k} profile of this function is shown in Fig. 6(a).

The energy of the free problem $E_0^{m,n}(\mathbf{k})$ together with the potential $V_{m,n;m',n'}$ defines an infinite matrix for each \mathbf{k}

$$H_{m,n;m',n'}(\mathbf{k}) = E_0^{m,n}(\mathbf{k})\delta_{m,m'}\delta_{n,n'} + V_{m,n;m',n'} \quad (\text{D5})$$

diagonalizing (D5) gives the spectrum of the antidot problem.

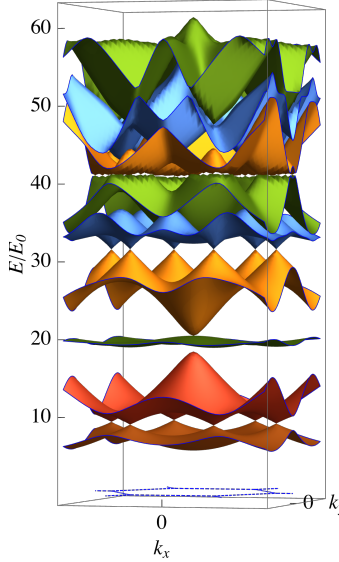


Figure 7. Dispersion in the non-flat regime, with values $(V_0/E_0, w/a_0) = (100, \sqrt{3}/2)$.

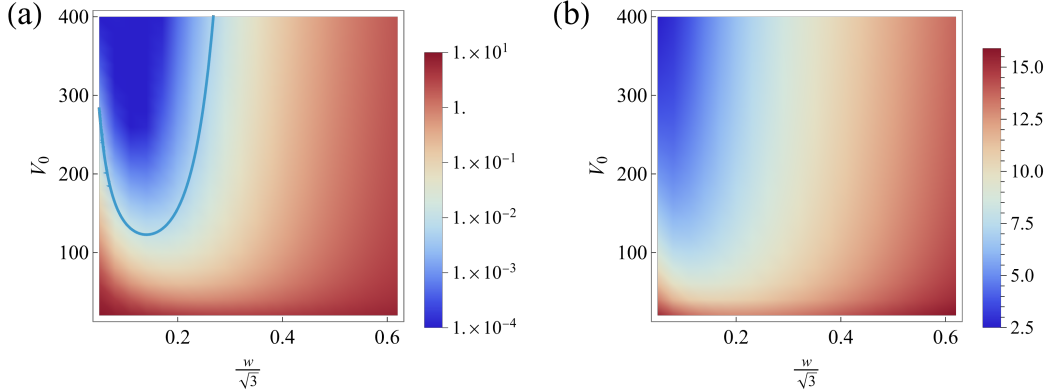


Figure 8. (a) The width of the approximately flat band (defined as the largest energy difference among the energy at momenta Γ , K , and M) as a function of w and V_0 ; the blue line marks the empirical line (D6) that divides between the flat and non-flat region. (b) The difference of the energy of the 2nd and the 1st bound states at the Γ point, as a function of w and V_0 . Note that the left is shown in logarithmic scale and the right in linear scale.

2. Numerical results

For the antidot problem, we choose the representative parameters $(V_0/E_0, w/a_0) = (400, \sqrt{3}/200)$ (the one used in the main text) and obtain the full spectrum in the entire Brillouin zone, as shown in Fig. 6(b). We also show a zoom-in view of the lowest two bands in Fig. 6(c), and plot the wave functions corresponding to the Γ points of these two bands in Fig. 6(d). The two wave functions ψ_0, ψ_1 correspond to the bound states localized at the junctions of the hexagonal channels. The junctions effectively behave as 0D quantum dots and host localized states; the 1D channels connecting them introduce tunneling and hybridize the neighboring states: the symmetric superposition gives rise to the lowest energy state ψ_0 with a unique sign structure and no nodes along the bond, while the antisymmetric superposition gives the higher energy state ψ_1 with alternating sign structure at the adjacent vertices and one node per bond.

For comparison, we also show the spectrum for the parameters $(V_0/E_0, w/a_0) = (100, \sqrt{3}/2)$ in Fig. 7. In this regime, the third lowest band becomes clearly dispersive; this band can be adiabatically traced to the third lowest band in Fig. 6(b) which is approximately flat. The bands at higher energies can be adiabatically traced to the parabolic band of the 2DEG in absence of the potential upon unfolding of the Brillouin zone.

Finally, we show in Fig. 8(a) and (b) the width of the lowest approximately flat band (which is the third lowest band), $\Delta_{FB,1}$, and that of the lowest two bands, Δ_{BS} , respectively, as a function of w and V_0 . Here $\Delta_{FB,1}$ is defined as

the largest difference among the energies at momenta Γ , K , and M of the third lowest band, and Δ_{BS} is defined as the energy difference between the second and the first lowest bands at the Γ point. Both $\Delta_{\text{FB},1}$ and Δ_{BS} are smooth functions of V_0 and w and exhibit no discontinuities, yet the scaling behavior are quite different: $\Delta_{\text{FB},1}$ various on an exponential scale with V_0 and w while Δ_{BS} on a linear scale. These behaviors indicate that the third band and the first two bands acquire finite widths through different tunneling processes: for $\Delta_{\text{FB},1}$, it is the tunneling between CLSs across the antidot barrier, which according to a WKB argument scales as $\sim \exp(-\sqrt{V_0})$; for Δ_{BS} , it is the hybridization of 0D modes which depends algebraically on V_0 and w .

To further characterize the flatness $\Delta_{\text{FB},1}$, we seek to separate the region in the parameter space (V_0, w) with approximately flat bands and the region without. A good practical criterion is $\Delta_{\text{FB},1} \leq 10^{-2}$, and we find an empirical curve that achieves this

$$\boxed{\sqrt{V_0 - 80 - 1.5/w^2}(\sqrt{3} - w)^9 = 150}. \quad (\text{D6})$$

The line is shown in Fig. 8(a).